A silicon micromechanical resonator with capacitive transduction for enhanced photoacoustic spectroscopy

Wioletta Trzpil, Julien Charensol, Diba Ayache, Nicolas Maurin, Roman Rousseau, Aurore Vicet, Michael Bahriz

Sensors & Actuators: B. Chemical xxx (xxxx) xxx

Contents lists available at ScienceDirect

Sensors and Actuators: B. Chemical

journal homepage: www.elsevier.com/locate/snb

A silicon micromechanical resonator with capacitive transduction for enhanced photoacoustic spectroscopy

Wioletta Trzpil [a], Julien Charensol [a], Diba Ayache [a], Nicolas Maurin [a], Roman Rousseau [a], Aurore Vicet [a], Michael Bahriz [a,*]

[a] IES, Univ. Montpellier, CNRS, F-34000 Montpellier, France

ARTICLE INFO

Keywords:
Photo-acoustic
Gas sensor
MEMS
Capacitive transduction
Micro-mechanical resonator
Spectroscopy

ABSTRACT

This paper presents the design of a silicon micromechanical resonator with capacitive transduction for a gas sensor based on photoacoustic spectroscopy. It overcomes problems imposed by opposite physical trends originating from the sensor's working principles. The capacitive transduction mechanism is considered incompatible with the photoacoustic gas detection as it reduces the mechanical displacement by a damping effect, thus decreasing the sensitivity. This occurs because the same part serves two functions: photoacoustic excitation and capacitive transduction. The suggested approach in this study focuses on the spatial separation of these two functions. We propose the first reported mechanical microresonator for photoacoustic gas sensing, which decouples photoacoustic excitation and capacitive transduction. The design has been modeled, fabricated, characterized, and compared with the on-beam Quartz-Enhanced Photoacoustic Spectroscopy (QEPAS) technique, a reference for compact and selective gas sensors. The performed photoacoustic measurement has been realized on calibrated concentrations of methane. For a 1 s integration time in first harmonic detection, we obtained a limit of detection (LOD) of 667 ppmv for silicon microresonator. In comparison to on-beam QEPAS technique, we obtained LOD of 163 ppmv, which constitutes a factor 4 between QEPAS and MEMS. The conditions for both experiments were the same.

1. Introduction

The constantly growing field of applications, for instance medicine [1], industry [2], security and defense [3], is boosting the gas sensors market. For most applications, gas sensors need to be selective, sensitive, demonstrate real-time measurement ability, and compact. Selectivity refers to the ability to identify a species among others, while sensitivity refers to the ability to reach part-per-million (ppm) detection level (e.g. [1]). The gas sensing market can be divided into four main techniques: electrochemical, semiconductors, infrared, and others (e.g., catalytic, thermal,.). Infrared sensors and in particular sensors based on optical methods like tunable laser diode spectroscopy (TDLS), are compelling due to their fast response, excellent selectivity, and sensitivity: reaching sensitivity up to ppb [4]. They do not require sample preparation. However, due to a sensitivity proportional to the optical path, their size-reduction is limited.

In photoacoustic spectroscopy, the signal is proportional to the power of the laser. This fact permits reducing sensor size in comparison with sensors based on direct absorption while maintaining similar performances. In photoacoustic spectroscopy, [5,6] the gas is detected through the absorption of the modulated laser light by the targeted gas. This absorption creates an acoustic wave that sets a mechanical resonator in motion. Currently existing mechanical resonators for photoacoustic wave detection are: non-resonant membrane such as microphone [7], resonant with piezoelectric transduction mechanism, called QEPAS technique (Quartz-Enhanced Photoacoustic Spectroscopy) [8]; and cantilever with interferometric transduction mechanism called CEPAS technique [9] (cantilever-enhanced photoacoustic spectroscopy). An acoustic chamber is required for CEPAS and standard photoacoustic with a microphone to increase photoacoustic pressure and make this method efficient. However, acoustic chambers are also used to improve the sensitivity of QEPAS [12].

Integration of the sensor with the CMOS technology is another requirement that needs to be met to develop compact gas sensors. Besides the potential of integration, silicon technology enables precise dimension control and batch production at a cheap cost with high

* Corresponding author.
E-mail address: michael.bahriz@umontpellier.fr (M. Bahriz).

https://doi.org/10.1016/j.snb.2021.131070
Received 9 July 2021; Received in revised form 21 October 2021; Accepted 4 November 2021
Available online 15 November 2021

repeatability. Therefore, it appears to be the most reasonable to develop a mechanical resonator based on silicon material like CEPAS or a microphone. The main drawback of standard photoacoustic gas sensors based on microphones comes from the need for a resonant acoustic chamber. In contrast, CEPAS sensors are relatively bulky due to the optical readout mechanism, and their further miniaturization is somewhat limited.

Therefore, a silicon micro-resonator with capacitive transduction mechanisms stands out as a promising solution. The operation principles of such a sensor are outlined in [13] while the concept was initially proposed by Chamassi et al. [14]. Silicon gives an excellent opportunity for integration while capacitive detection provides simplicity and has been proven to be highly sensitive [15]. Compared to standard photoacoustic, the advantage of this solution is using a mechanical resonator with a high quality factor that acts as a band-pass filter. It allows to avoid an acoustic chamber and reduce the sensor size.

The main challenge in creating a sensitive capacitive microresonator-based sensor for photoacoustic gas detection comes from the transduction mechanism itself. In capacitive transduction, the electric signal is inversely proportional to the distance between the electrodes. For instance, in our case, a gap 3 μm was used. This proximity between electrodes creates important viscous damping called squeeze film effect [16]. To decrease this damping, the width of the structure should be decreased. On the other hand, the surface, and thus the width, needs to be increased to increase the acoustic force. This creates a dilemma since it is necessary to increase the width for photoacoustic force enhancements, while for viscous damping reduction, it is necessary to decrease the width. Therefore, we assert that optimizing for photoacoustic force collection of a mechanical resonator with capacitive transduction exhibits an opposite trend than optimizing for viscous damping reduction. Article [13] aimed to find geometrical parameters of a cantilever that would represent a compromise between these two opposite trends and enhance the capacitive signal. However, despite this optimization, a simple cantilever based on SOI (silicon on insulator) wafers will not reach the same performance as a quartz tuning fork.

Our research aims to create a high-performance silicon micromechanical resonator for photoacoustic gas detection with capacitive transduction. To reach this objective, we have developed a design of a complex mechanical resonator, presented in Fig. 1. Due to its shape, it will be further called H-resonator. The H-resonator is divided into several parts: the first part (zone 1) is designed to maximize the photoacoustic energy collection, the second (zones 2) is designed to maximize the capacitive transduction.

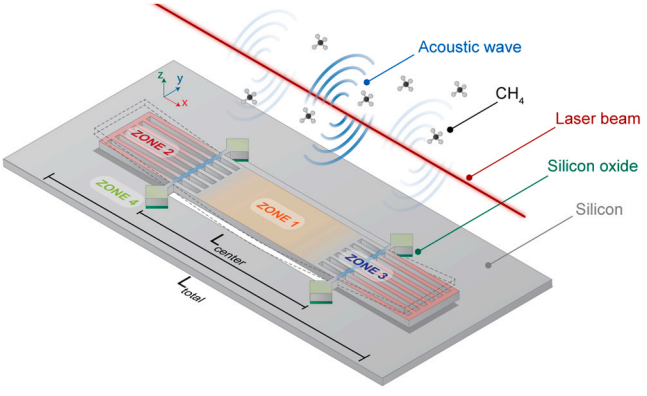

Fig. 1. Scheme of H-resonator with a schematic illustration of the deflection under PA excitation. The laser beam is localized along the resonator (x-axis) while its focal point is above the middle of the resonator. The acoustic wave is created along the beam due to the absorption of modulated light. Zone 1 collect the photoacoustic energy. Zone 2 is used for the capacitive transduction. Zone 1 and 2 are connected by zone 3, called 'junction'. Zone 4, called anchor, holds all the structure.

The working principle is the same as presented in [13]. The laser beam is localized along the resonator while its focal point is above the middle of zone 1 (Fig. 1). The acoustic wave is created along the beam due to the absorption of modulated light. Absorption will occur if the laser wavelength corresponds to the absorption line of a target gas (methane in our study). The device is fabricated on an SOI (Silicon-on-Insulator) wafer composed of three layers: 75 μm thick silicon, which creates a device layer, followed by 3 μm thick box layer made of silicon oxide, and 400 µm thick silicon substrate. The resonator is fabricated in the device layer and consequently has a thickness of 75 μm. When it is set in motion by the acoustic wave, it creates a movable electrode. The capacitance variation due to the resonator's displacement can be transformed into a current or voltage signal, depending on the resonator's frequency [17–19] and the external electrical circuits.

The resonator design has been developed using the analytic model presented in [13] and combined with COMSOL simulations. It has been fabricated in cleanroom facilities. Photoacoustic spectroscopy performance demonstrations have been realized on methane. It is a very potent greenhouse gas generated in high quantity by the agri-food sector. It is also well-known near-infrared spectroscopic reference gas.

In this paper, section 2 presents the concept and explains the H-resonator geometry. Section 3 concerns the fabrication process. Section 4 presents the setup for photoacoustic gas detection, characterization for QTF and H-resonator, first and second harmonic detection (1f and 2f detection) of a methane line, linearity of on-beam QEPAS and H-resonator based sensor, and the limit of detection using Allan variance for both on-beam QEPAS and H-resonator. Section 5 presents and compares normalized noise equivalent absorption coefficient NNEA for on-beam QEPAS and H-resonator.

2. Silicon micro resonator design

2.1. Concept of coupled resonators

As we presented in [13] opposite trends characterize the geometry optimization of the capacitive cantilever for photoacoustic gas detection. These opposite trends make it impossible to reach a sensitivity at the state-of-the-art using just a simple cantilever. To overcome this problem, a different approach needs to be applied. Our solution focuses on separating problems into different parts. We have created a structure where parts for photoacoustic energy collection and electrical transduction can be optimized separately. As presented in Fig. 1, the resonator is divided into four mechanical zones, which fulfill the following functions: capacitive transduction, acoustic energy collection, mechanical coupling, and support for the structure.

The geometry of the orange part called zone 1 in Fig. 1 has been chosen to collect photoacoustic energy along the resonator as the photoacoustic wave will be created along the laser beam. It collects the photoacoustic force to set the whole structure in motion. It must be characterized by a significant overlapping between the mechanical mode and the acoustic wave to enhance energy collection. We added a hole below this part to decrease the viscous damping and particularly avoid the squeeze film effect.

Red zone 2 in Fig. 1, represents areas where the mechanical movement is converted into an electrical signal via capacitive transduction. It is composed of several long and thin clamped-free cantilevers. The electrical signal is proportional to the capacitance variation of this area, which is proportional to the distance variation between the mobile and the fixed electrode (top part of the resonator and the substrate). In the presented design, the two electrodes are 3 μm apart (oxide layer in Fig. 1) to work with sufficiently large capacity. This proximity traps a thin air film between the electrodes generating additional viscous damping called squeeze film damping [16]. This effect cannot be avoided, although it can be reduced. To minimize it, we used a clamped-free cantilever in the fundamental mode of vibration to modelize the long arms in zone 2. Subsequently, we applied the analytic model [13] and

estimated that the lowest damping/higher displacement would be obtained for a width around 12 μm. The numerous arms are used to maximize the resonator's nominal capacitance. The presented design (Fig. 1) has ten arms on each side of the resonator.

Blue zone 3 marked in Fig. 1, further called "junction", is the mechanical part connecting zones 1 and 2. Its position along the x-axis (resonator's length) defines the coupling between zones 1 and 2.

Zone 4 called "anchor" is designed to hold the whole structure and reduce mechanical losses into the support. Its geometry is a square rotated by 45 degrees relative to the other part of the H-resonator. It has been optimized by finite element simulation to minimize the proportion of the total energy dissipated into the substrate. The support size of 250 µm x 250 µm stands a good compromise as it allows holding all the structure while maintaining relatively small parasitic capacitance and support losses.

2.2. Structure optimization

To optimize the electrical output under the photoacoustic force excitation, it is necessary to increase the photoacoustic energy collection and maximize the displacement for zone 2 as the capacitive signal is proportional to displacement variation. One approach for increasing displacement is to reduce the effective mass m_{eff}. Zone 2 is composed of 12 μm width cantilevers separated with distance of 75 μm. Zone 1 is characterized by high mass compared to zone 2 due to the large surface for photoacoustic energy collection. It can increase the effective mass of the resonator if its displacement is high. Low effective mass can achiever by reducing the maximal amplitude of displacement of zone 1 max (W_{zone1}), and maximize the maximal displacement of zone 2 max (W_{zone2}). This approach allows to simultaneously increase the electric signal and decrease the effective mass.

We have studied the ratio of displacement W_{ratio} between the maximal amplitude of displacement of zone 1 max(W_{zone1}) and the maximal amplitude of displacement of zone 2 max(W_{zone2}): $W_{ratio} = max(W_{zone2})/max(W_{zone1})$ as a function of the ratio L_{center} / L_{tot}. Where L_{center} is the distance between anchors (zone 4) and L_{total} is the total length of the resonator, which remain constant $L_{tot} = 4700\mu m$ (Fig. 1). Studies were performed using COMSOL multiphysics software based on finite element simulation. The simulation results presented in Fig. 2 show that it is possible to maximize W_{ratio} and simultaneously decrease the effective mass. The blue circle indicates the value $L_{center}/L_{total} = 0.52$, which was used for the resonator presented in this paper. For this value, the effective mass is $m_{eff} = 25\ \mu g$ and ratio of displacement $W_{ratio} = 4$. While it is possible to reach a higher ratio of displacement and lower effective mass by decreasing the value of L_{center} / L_{tot} it has been chosen not to use value under 0.52. Indeed for value below 0.50 simulations show that the distance between the different mechanical mode is lower than 5 kHz. This domain corresponds to the brown curves in Fig. 2. If another mode is too close to the mode of interest, a cross talk can appear and reduce the amount of energy in the mode of interest.

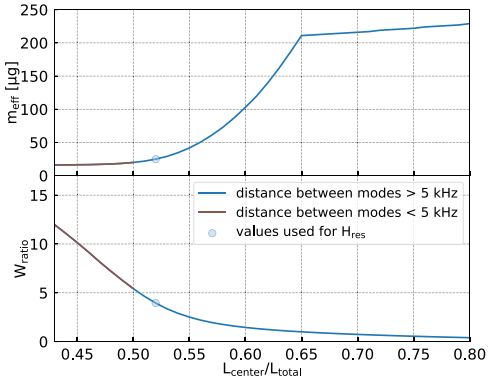

Fig. 2. Results from simulation presenting an effective mass m_{eff} and ratio of displacement W_{ratio} between the two maximum amplitude of displacement of zone 1 max(W_{zone1}) and of zone 2 max(W_{zone2}): $W_{ratio} = max(W_{zone2})/max(W_{zone1})$ as a function of L_{center} / L_{tot}, where L_{center} is the distance between anchors (zone 4) and $L_{tot} = 4700\ \mu m$ is total length of the resonator. The blue circle indicates the value used for the resonator presented in this article. It corresponds to the $m_{eff} = 25\ \mu g$ and ratio of displacement $W_{ratio} = 4$. Simulation were made using COMSOL multiphysics software for this fundamental mode of vibration.

3. Sample fabrication

The device was fabricated on a double-side polish, (100) oriented silicon-on-insulator (SOI) wafer. It consists of a 400 μm thick substrate with a resistivity of 0.01–0.02 (Ω cm), a 3 μm thick SiO_2 layer, and a 75 μm thick device layer with a resistivity of 0.01–0.02 (Ω cm). Both sides of the wafer were covered with 320 nm (-+5 nm) of low stress silicon nitride SiN_x [20] deposited by LPCVD (Low-Pressure Chemical-Vapour Deposition) technique. Steps for device fabrication are presented in the Fig. 3.

The first step of the fabrication process consists of a deep wet etching on the back of the wafer using 22%wt KOH solution at 60 °C. After back etching, photolithography is performed to define the mechanical resonator on the top side of the SOI wafer. The cavity needs to be aligned with a resonator pattern on the opposite side of the wafer. This process is subject to alignment uncertainty, as shown in Fig. 4.

After the opening of the photolithography resist and SiN_x mask, the mechanical resonator is etched using the standard Bosh process [21]. This step of the process was conducted in the FEMTO-ST Institute (Besancon, France). The buried silicon oxide layer was etched using vapor hydrofluoric acid following the procedure detailed in [22] creating a free-standing structure. We used highly doped silicon to avoid any metal deposition and connected the MEMS with an aluminum wire bonding. Fig. 4 presents the final device with its wire bonding.

4. Methods and experiment

In this section, we present the results of sensor performance and compare them with the standard on-beam QEPAS technique. This comparison is significant as the QEPAS stands as one of the best techniques in terms of sensitivity in photoacoustic gas sensing.

Primarily, both H-resonator and QEPAS need to be characterized. Based on this characterization, we estimate the resonance frequency and quality factor. The laser will be modulated at the resonance frequencies of each transducer to maximize the electric signal from photoacoustic gas detection. The experimental setup, presented in the Fig. 5, involves a NORCADA commercial distributed feedback (DFB) laser emitting around 4300 cm^{-1} in a continuous wave regime. Within this emission

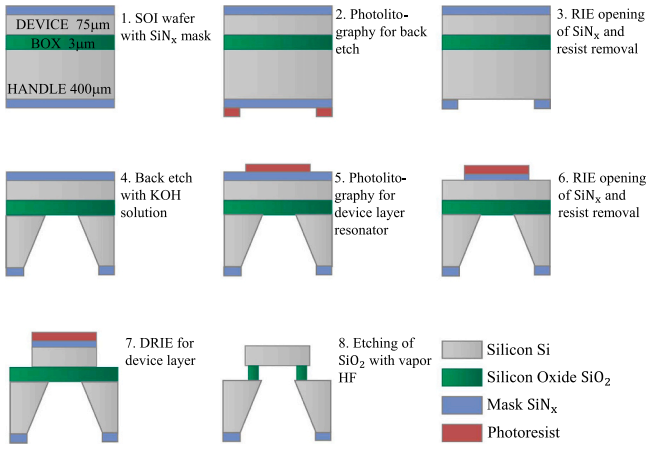

Fig. 3. Steps for the sample fabrication.

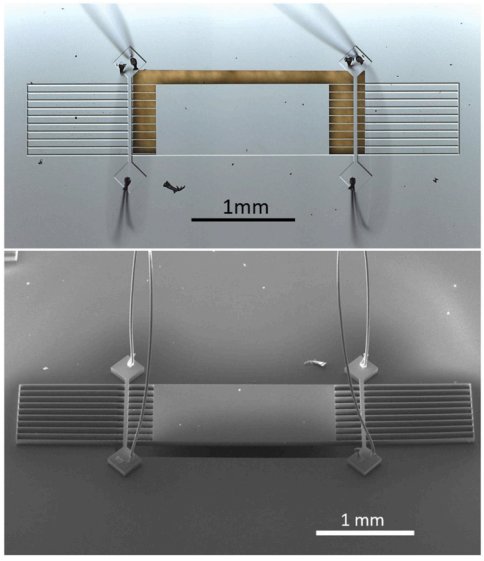

Fig. 4. Optical (upper panel) and scanning electron microscopy (lower panel) pictures of a silicon micro-mechanical resonator (H-resonator) with its wire bonding. The resonator has the following dimensions: length 4700 μm, width 775 μm and thickness 75 μm.

range exists a strong and isolated transition of methane, based on HITRAN Database [23], at $\nu = 4300.36$ cm^{-1} with absorption cross-section $\sigma = 3.7 \cdot 10^{-}21$ cm^2 molecule^{-1}. A Thorlabs Laser Driver ITC4002QCL LDITC regulates the laser diode temperature and current. The laser's current threshold reaches 40 mA at 25 °C. An MFLI Lock-in Amplifier modulates the laser current. The laser light is collimated in the chamber equipped with a gas inlet, outlet, and CaF_2 window tilted at 20^o to prevent interferences and feedback into the laser. In the cell, the beam is focused above the resonator, in the case of the H-resonator, and between the prongs of QTF in a bare QEPAS configuration. The acoustic wave generated by the modulated light absorption causes the mechanical movement of the QTF or H-resonator. The electric signal from QTF is generated by the piezoelectric effect. Then, the signal is processed by a transimpedance amplifier with 10^8 gain and demodulated at the laser modulation frequency using the lock-in amplifier. To generate an electrical signal from the displacement of the silicon microresonator with capacitive transduction, the resonator needs to be primarily polarized with a bias V_{DC}. The current from the resonator is then amplified and converted into voltage using a FEMTO current amplifier LCA-40 K-100 M. The amplified signal is subsequently demodulated at laser modulation frequency using MFLI lock-in amplifier. All the experiments were conducted at atmospheric pressure.

4.1. Characterization

To characterize the QTF and H-resonator, we target a methane absorption peak at $\nu = 4300.36$ cm$^{-}1$. Accordingly, the laser temperature is fixed at 25 °C and current at 138.5 mA. To obtain a photoacoustic signal, we use the wavelength modulation spectroscopy (WMS) [24]. We performed a frequency sweep over the laser light modulation to characterize and get the frequency response from QTF and H-resonator. Based on the conducted experiment, the resonance frequency of the QTF is found to be at $f_0 = 32.7$ kHz while the quality factor 13,000. The frequency response of H-resonator was measured under different polarisation biases. Fig. 6 presents the main mechanical resonance for different polarization voltage and their Lorentzian fit. The second visible peak on the left of the main resonance is another mechanical mode of the resonator.

As expected, the electrical signal is proportional to the polarization voltage. For low polarisation voltages, the response of H-resonator can be described by a Lorentzian curve. The Lorentzian fit gives a resonance frequency for H-resonator, which amounts $f_0 = 44.79$ kHz and a quality factor $Q = 266$. The resonance frequency shift with the polarization voltage is due to a change of spring constant caused by the electrostatic

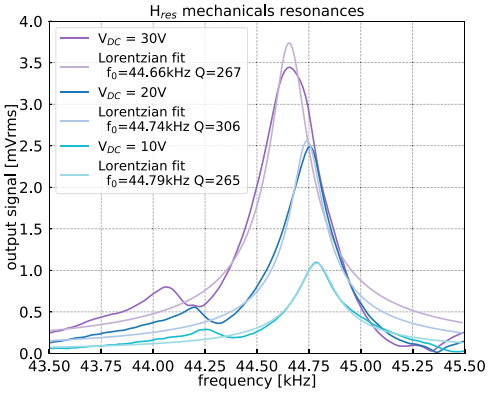

Fig. 6. Capacitive measurement of H-resonator frequency response with 100% of CH_4 for different polarisation voltage V_{DC}. The quality factor and the resonance frequencies were obtained via Lorentzian fit.

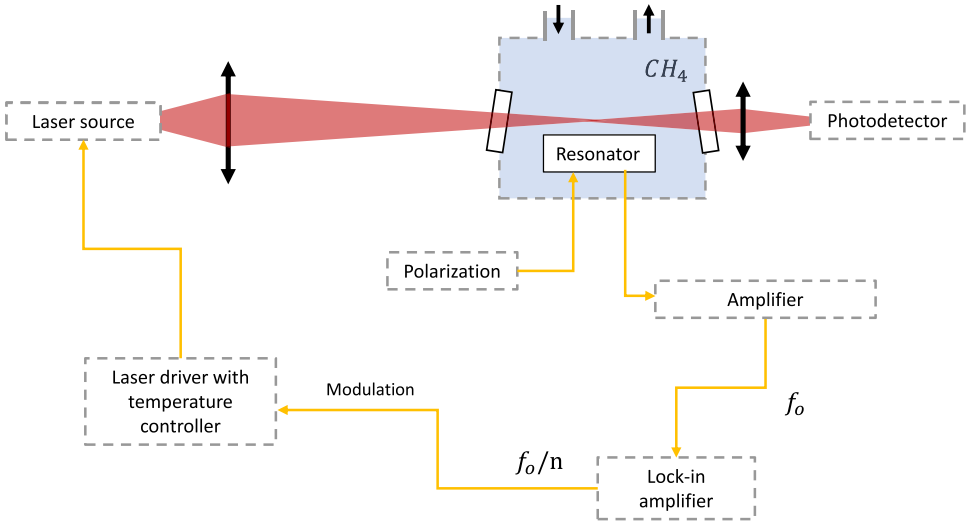

Fig. 5. Scheme of the experimental setup which can be used for direct absorption spectroscopy (with photodiode) and photoacoustic spectroscopy (with mechanical resoantor). The laser current is modulated at n-harmonic (n = 1 for 1f detection, n = 2 for 2f detection). The signal from the resonator is demodulated by the lock-in amplifier. The setup presented in this figure allows to identify the gas absorption line via direct absorption using photodetector and via photoacoustic wave detection using the mechanical resonator.

force acting on the resonator. To maximize the electric signal from the H-resonator, the following measurements are performed with a polarization voltage of 30 V. It is worth noticing that high polarisation voltage may cause a collapse of the resonator [25].

4.2. Gas detection

According to wavelength modulation theory, the amplitude of the laser modulation is a significant parameter for photoacoustic signal maximization [24]. An optimum is attained by increasing the modulation amplitude of the laser, yielding the optimal modulation amplitude, which is 9.1 mA and 9.3 mA for first and second harmonic detection (1f and 2f detection), respectively. The silicon micromechanical resonator is sensible to photo-thermal excitation. This kind of excitation can bring a false positive electrical signal even without the presence of the target gas as it will cause the movement of the resonator. To verify if the signal comes from photoacoustic excitation, we performed detection of the first and second derived of the gas spectrum. This corresponds to 1f and 2f detection.

To identify the 1f and 2f signatures of the target gas absorption, we used setup presented in Fig. 5 which can be used for direct absorption spectroscopy (with photodiode) and photoacoustic spectroscopy (with mechanical resoantor). For 1st harmonics (n = 1) the laser is modulated at resonance frequency of the mechanical resonator f_0; while for 2nd harmonics (n = 2) laser is modulated at half frequency of the resonator $f_0/2$. The cell was filled up with 10% CH_4 diluted in pure nitrogen and a spectral scan was performed by tuning the driving current between 136 mA and 145 mA. As presented in [24], a smaller modulation amplitude will result in clear first and second derivative of the absorption spectrum. We used a modulation amplitude of 6.7 mA for 1 f and 7.5 mA for 2 f detection for clear identification of their signature. Subsequently, we compared the 1f and 2f detection to absorption spectra obtained by the photodiode measurement with 100% CH_4 and without the gas. The measurements are presented in the Fig. 7 and confirm the photoacoustic excitation of the resonator.

Subsequently, we performed a linearity measurement on a calibrated dilutions of CH_4 obtained using a mass flow controller Alytech GasMix Aiolos II. This measurement provides information about the linearity and proportion between photoacoustic and photothermal excitation as the signal is also measured without the presence of absorbing gas. The signal measured without the presence of absorbing gas gives information about the photothermal noise. Fig. 8 presents results form linearity measurement. The curves were evaluated by monitoring the 1f signal from both the QTF and the H-resonator in dynamic measurement with a gas flow rate 950 Nml/min. The cell was gradually filled with a calibrated gas concentration and flushed with pure N_2 between each stage to confirm the recovery of the zero signal. Each step was performed for 10 min, and the measurement was recorded continuously. Both curves present fair and similar linearity, which indicated a lack of sensor nonlinearity caused by high voltage bias. There is a noticeable offset in the QTF data, which is the result of thermal excitation. This photothermal excitation was minimized in the further measurement through the improvement of the setup alignment. It is worth noticing that 2f detection minimizes the photothermal noise.

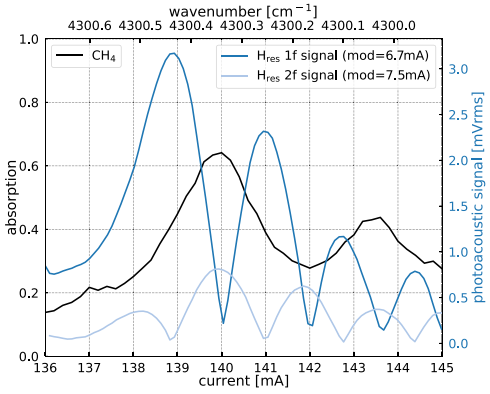

Fig. 7. Absorption spectra of methane obtained by photodiode measurement with 100% CH_4 and without gas (black curve) on an optical path of 3 cm. The absolute value of 1st (light-blue) and 2nd (dark blue) harmonic - WMS signal obtained by the absorption of 10% CH_4 at atmospheric pressure, using a DFB laser emitting around 2.3 μm with an output power of 3.9 mW for a current of I = 140 mA at a temperature of 25 °C.

4.3. Allan-Werle deviation

To evaluate the sensitivity and stability of the sensors, we performed an Allan-Werle variance analysis [26] for data series collected during 30 min at CH_4 concentration of 10% and time constant of 100 ms. Allan variance was performed by monitoring 1f and 2f signals for the quartz tuning fork and the H-resonator with an optimal modulation amplitude: 9.1 mA and 9.3 mA for 1f and 2f detection. To reach the maximal signal, the current was fixed at I = 138.5 mA and I = 140 mA for 1f and 2f detection, respectively. For these conditions, the laser power reaches 3.86 mW and 3.92 mW, respectively. The results are presented in the Fig. 9. The slope of the curve given for integration time $\tau < 1$ s does not show the behavior of expected classical $t^{-1/2}$ slope. This behavior is related to the lock-in amplifier low pass filter and its cut-off frequency. It is assumed that the measurement will be reliable for τ at least 5 times higher than the time constant. It indicates that if the Allan variance was applied to data with a time constant, for instance, 100 ms, the results would be reliable and should present classical $t^{-1/2}$ slope for τ higher than $\tau = 500$ ms. As a result, the curves in Fig. 9 have a conventional $t^{-1/2}$ slope for $\tau > 1$ s. The long-term drift appears after the 40 s for QTF, while for H-resonator after 55 s and 105 s for 1f and 2f detection, respectively.

According to the 1σ criteria, the CH_4 limit of detection (LOD) for silicon micromechanical resonator is 667ppmv at 1 s integration for 1f detection and improves to 264ppmv for 10 s of integration. For 2f detection, LOD amounts 789 ppmv for 1 s of integration and 283ppmv for 10 s of integration.

In comparison to QEPAS on-beam configuration, LOD for 1f detection amounts 163 ppmv and 66 ppmv for integration time 1 s and 10 s, respectively; while for 2f detection 265 ppmv and 100 ppmv for integration time 1 s and 10 s, respectively.

5. Discussion and conclusions

Our objective was to develop a high-performance silicon microresonator with capacitive transduction for photoacoustic gas sensing. Capacitive transduction in photoacoustic gas sensors based on micromechanical resonators is limited by the opposite physical trends of the sensor's working principles. In this paper, we proposed and applied a method that solves this problem. We have designed and fabricated the first silicon microresonator for photoacoustic gas sensing, decoupling photoacoustic excitation from capacitive transduction. We demonstrated linear response for gas detection conducted on calibrated methane concentration.

It is possible to theoretically estimate the difference of performances between the H-resonator and an optimized cantilever fabricated on the same SOI wafer and operating at the same resonance frequency using an analytic model presented in [13]. According to this model, an optimized cantilever based on a SOI wafer of 75 μm with a box of 3 μm should have a width of 11 μm and a length of 1,42 mm. By taking into account only the Brownian noise, the cantilever should present a signal-to-noise ratio of 11 against a signal-to-noise ratio of 150 for the H-resonator for the first harmonic detection with 1 s of integration time. While this comparison is not as reliable as an experimental one, it indicates that the performances increase with H-resonator.

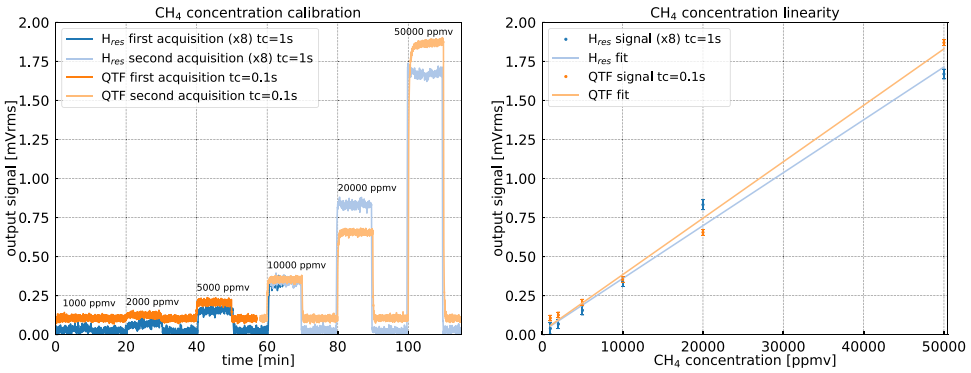

Fig. 8. a)1f QEPAS (orange) and H-resonator (blue) signal during a gas step cycle, with concentration ranging from 1000 ppmv to 50000ppmv. The methane mixture of known concentration is injected for 10 min, and the cell is flushed with pure N_2 for the next 10 min. (b)QEPAS (orange) and H-resonator (blue) signal versus injected methane concentration with a linear fit (right panel) of the response. The integration time is set to 1 s for H-resonator and 0.1 s for QEPAS.

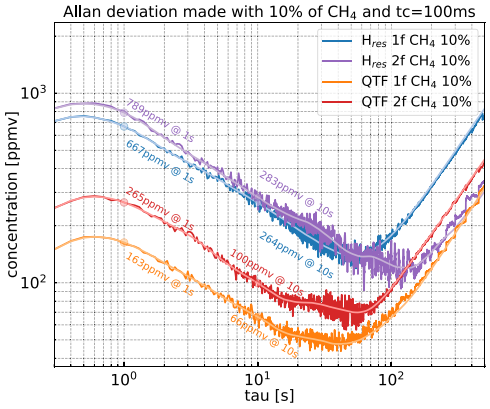

Fig. 9. Allan-Werle deviation calculated from a 30 min acquisition for the 1f and 2f mode with 10% of CH_4 concentration and time constant of 100 ms.

The H-resonator LOD for 1f detection at 1 s integration time leads to a normalized noise equivalent absorption coefficient (NNEA) of $5.5 \cdot 10^{-7}$ W cm^{-1} Hz$^{-1/2}$. In comparison, for QEPAS NNEA at 1 s integration amounts $1.3 \cdot 10^{-7}$ W cm^{-1} Hz$^{-1/2}$. The NNEA for the first reported on-beam QEPAS amounts $8.8 \cdot 10^{-7}$ W cm^{-1} Hz$^{-1/2}$ [8]. Presented NNEA for QEPAS constitutes better results than NNEA for resonant MEMS by factor 4. Both measurements were conducted in the same conditions, which indicates the high reliability of the results. The vibrational-transitional relaxation time for CH_4 is around 11.5 μs [27]. As presented in [13] the maximum of the acoustic force should be around 11 kHz. Thus, with their respective resonance frequency of 44.7 and 32 kHz the H-resonator and the quartz tuning fork are subjected to almost the same acoustic pressure. For a gas with a slower vibrational-transitional relaxation time, the LOD for both sensors will be worse due to the shift of the maximum of the acoustic pressure at lower frequencies [13].

Although the silicon-based microresonator is in its early stage of development, its performances are comparable to the on-beam QEPAS performances.

The sensor's future developments will focus on design improvement to increase the quality factor and photoacoustic energy collection. With the design improvement, it appears that achieving the same or superior sensitivity to QEPAS-based sensors is feasible. We believe that the development of the silicon microresonator presented in this paper paves the way for a new generation of integrated gas sensors.

CRedit authorship contribution statement

W.T. was in charge of the methodology and the investigation, under the supervision of A.V. and M.B. She was assisted by J.C., N.M. and D.A. for data curation. The article was written by W.T. and M.B., reviewed by A.V. All authors have read and agreed to the published version of the manuscript.

Declaration of Competing Interest

The authors declare that they have no known competing financial interests or personal relationships that could have appeared to influence the work reported in this paper.

Acknowledgement

This research was financially supported by the French Ministry of Defense (DGA-MRIS), Region Languedoc Roussillon, European Community (FEDER) and Renatech, Agence Nationale de la Recherche, France (MULTIPAS Project No. [ANR-16-CE04–0012], and NOMADE Project No. [ANR-18- CE04–0002-01]).

References

[1] N. Maurin, R. Rousseau, W. Trzpil, G. Aoust, M. Hayot, J. Mercier, M. Bahriz, F. Gouzi, A. Vicet, First clinical evaluation of a quartz enhanced photo-acoustic CO sensor for human breath analysis, Sens. Actuators, B: Chem. 319 (2020), 128247.
[2] M.E. Webber, T. MacDonald, M.B. Pushkarsky, C.K.N. Patel, Y. Zhao, N. Marcillac, F.M. Mitloehner, Agricultural ammonia sensor using diode lasers and photoacoustic spectroscopy, Meas. Sci. Technol. 16 (8) (2005) 1547–1553.
[3] A.I. Karapuzikov, S.S. Nabiev, A.I. Nadezhdinskii, Y.N. Ponomarev, Laser methods of detecting vapor explosives in the open atmosphere: analytical possibilities for counteracting terrorist acts, Atmos. Ocean. Opt. 24 (2) (2011) 133–143.
[4] K. Namjou, S. Cai, E.A. Whittaker, J. Faist, C. Gmachl, F. Capasso, D.L. Sivco, A. Y. Cho, Sensitive absorption spectroscopy with a room-temperature distributed-feedback quantum-cascade laser, Opt. Lett. 23 (3) (1998) 219.
[5] P. Patimisco, G. Scamarcio, F.K. Tittel, V. Spagnolo, Quartz-enhanced photoacoustic spectroscopy: a review, Sensors 14 (4) (2014) 6165–6206.
[6] M. Duquesnoy, Tuning forks in photoacoustic spectroscopy: Comparative study and new developments. PhD thesis, Université Paris-Saclay, 2021.
[7] S.L. Castleden, G.F. Kirkbright, D.E. Spillane, Wavelength modulation in photoacoustic spectroscopy, Anal. Chem. 53 (14) (1981) 2228–2231.
[8] A.A. Kosterev, Y.A. Bakhirkin, R.F. Curl, F.K. Tittel, Quartz-enhanced photoacoustic spectroscopy, Opt. Lett. 27 (21) (2002) 1902–1904.
[9] V. Koskinen, J. Fonsen, K. Roth, J. Kauppinen, Cantilever enhanced photoacoustic detection of carbon dioxide using a tunable diode laser source, Appl. Phys. B: Lasers Opt. 86 (3) (2007) 451–454.
[10] H. Lv, H. Zheng, Y. Liu, Z. Yang, Q. Wu, H. Lin, B.A.Z. Montano, W. Zhu, J. Yu, R. Kan, et al., Radial-cavity quartz-enhanced photoacoustic spectroscopy, Opt. Lett. 46 (16) (2021) 3917–3920.
[11] W. Trzpil, N. Maurin, R. Rousseau, D. Ayache, A. Vicet, M. Bahriz, Analytic optimization of cantilevers for photoacoustic gas sensor with capacitive transduction, Sensors 21 (4) (2021) 1–22.
[12] K. Chamassi, W. Trzpil, R. Arinero, R. Rousseau, A. Vicet, M. Bahriz, Capacitive silicon micro-electromechanical resonator for enhanced photoacoustic spectroscopy, Appl. Phys. Lett. 115 (8) (2019).
[13] U. Ferlito, A.D. Grasso, S. Pennisi, M. Vaiana, G. Bruno, Sub-femto-farad resolution electronic interfaces for integrated capacitive sensors: a review, IEEE Access 8 (2020) 153969–153980.

[14] M. Bao, H. Yang, Squeeze film air damping in MEMS, Sens. Actuators A: Phys. 136 (1) (2007) 3–27.
[15] S. Meninger, J.O. Mur-Miranda, R. Amirtharajah, A.P. Chandrakasan, J.H. Lang, Vibration-to-electric energy conversion, IEEE Trans. Very Large Scale Integr. (VLSI) Syst. 9 (1) (2001) 64–76.
[16] P.R. Scheeper, A.G. van der Donk, W. Olthuis, P. Bergveld, A review of silicon microphones, Sens. Actuators. A Phys. 44 (1) (1994) 1–11.
[17] M. Bao, Analysis and Design Principles of MEMS Devices, Elsevier,, 2005.
[18] P. Temple-Boyer, C. Rossi, E. Saint-Etienne, E. Scheid, Residual stress in low pressure chemical vapor deposition SiNx films deposited from silane and ammonia, J. Vac. Sci. Technol. A: Vac., Surf., Films 16 (4) (1998) 2003–2007.
[19] F. Laermer, A. Schilp, and Robert Bosch GmbH, Method of anisotropically etching silicon, US Patent 5501893, p. US5501893 A, 1993.
[20] Y. Fukuta, H. Fujita, H. Toshiyoshi, Vapor hydrofluoric acid sacrificial release technique for micro electro mechanical systems using labware, Jpn. J. Appl. Phys., Part 1: Regul. Pap. Short Notes Rev. Pap. 42 (6A) (2003) 3690–3694.
[21] I.E. Gordon, L.S. Rothman, C. Hill, R.V. Kochanov, Y. Tan, P.F. Bernath, M. Birk, V. Boudon, A. Campargue, K.V. Chance, B.J. Drouin, J.M. Flaud, R.R. Gamache, J. T. Hodges, D. Jacquemart, V.I. Perevalov, A. Perrin, K.P. Shine, M.A. Smith, J. Tennyson, G.C. Toon, H. Tran, V.G. Tyuterev, A. Barbe, A.G. Császár, V.M. Devi, T. Furtenbacher, J.J. Harrison, J.M. Hartmann, A. Jolly, T.J. Johnson, T. Karman, I. Kleiner, A.A. Kyuberis, J. Loos, O.M. Lyulin, S.T. Massie, S.N. Mikhailenko, N. Moazzen-Ahmadi, H.S. Müller, O.V. Naumenko, A.V. Nikitin, O.L. Polyansky, M. Rey, M. Rotger, S.W. Sharpe, K. Sung, E. Starikova, S.A. Tashkun, J.V. Auwera, G. Wagner, J. Wilzewski, P. Wcisło, S. Yu, E.J. Zak, The HITRAN2016 molecular spectroscopic database, J. Quant. Spectrosc. Radiat. Transf. 203 (2017) 3–69.
[22] S. Schilt, L. Thévenaz, P. Robert, Wavelength modulation spectroscopy: combined frequency and intensity laser modulation, Appl. Opt. 42 (33) (2003) 6728.
[23] N. Tas, T. Sonnenberg, H. Jansen, R. Legtenberg, M. Elwenspoek, Stiction in surface micromachining, J. Micromech. Microeng. 6 (4) (1996) 385–397.
[24] P. Werle, R. Mücke, F. Slemr, The limits of signal averaging in atmospheric trace-gas monitoring by tunable diode-laser absorption spectroscopy (TDLAS), Appl. Phys. B Photophys. Laser Chem. 57 (2) (1993) 131–139.
[25] S. Schilt, J.P. Besson, L. Thévenaz, Near-infrared laser photoacoustic detection of methane: the impact of molecular relaxation, Appl. Phys. B: Lasers Opt. 82 (2) (2006) 319–329 (SPEC. ISS.).

Wioletta Trzpil is a PhD student at the Institute of Electronics and Systems (CNRS/University of Montpellier, France). She graduated from the Wrocław University of Science and Technology (Wrocław, Poland) in 2017, with a major in Technical Physics; specialization nanoengineering. Her current work focuses on development of micro-electro-mechanical systems (MEMS) for photoacoustic gas sensors.

Julien Charensol is a student at institutes of electronics and systems (CNRS / University of Montpellier, France). He is following a Master degree at the University of Montpellier in fundamental physics, nanosciences and functional materials. He is currently working on development of microelectro-mechanical systems (MEMS) for photoacoustic gas sensors.

Diba Ayache is a PhD student at Institutes of Electronics and Systems (CNRS/University of Montpellier, France). She graduated from the University of Montpellier with a Master's degree in electronics and medical devices engineering in 2020. She is currently working on the analysis of exhaled breath by infrared photoacoustic spectroscopy.

Nicolas Maurin is a former engineer at the Institute of Electronics and Systems (CNRS/University of Montpellier, France). He graduated from the ENSSAT (Lannion, France) with a major in Photonic, in 2019. He also graduated from the University of Montpellier with a major in Biophysics in 2019.

Dr. Roman Rousseau graduated from the National Institute of Applied Sciences (Rennes, France) in 2017, with a major in Applied Physics. He obtained his PhD in 2020 from the Institute of Electronics and Systems (CNRS/University of Montpellier, France) for his work on the development of Quartz Enhanced Photoacoustic Spectroscopy sensors for air quality monitoring and other applications employing Laser diodes and Quantum Cascade Lasers.

Dr. Aurore Vicet is an associate professor in Montpellier University, France, in charge of spectroscopic developments on tunable lasers: study and characterization of single frequency semiconductor lasers for spectroscopic applications in the infrared, study and development of TDLAS systems based on resonant photoacoustic techniques, Laser/LED quartz enhanced photoacoustic sensing, Si-based oscillators.

Dr. Michael Bahriz is an associate professor in Montpellier University, France. His main themes of research are the development of quantum cascade lasers based on InAs material system for the far infrared domain of the electromagnetic spectrum, and the development of MEMS on silicon specifically designed for the photo-acoustic gas detection.